Chapter 10
Element-Specific Spin States in Heusler-Alloy Compounds Probed by X-Ray Magnetic Spectroscopy

Jun Okabayashi, Kazuya Z. Suzuki, and Shigemi Mizukami

Abstract Recent progress of x-ray magnetic circular dichroism (XMCD) studies for Heusler alloy compounds which are expected as high spin-polarized materials is summarized. For some Heusler alloys forming X_2YZ compositions, where X and Y are transition-metal (TM) elements and Z is non-TM element, the element-specific magnetic properties by XMCD are investigated to understand the electronic structures. At first, a principle of XMCD spectroscopy is introduced. Second, the research interests in Heusler alloys are explained. Then, the results of XMCD for equatorial $XX'YZ$ composited Heusler-type spin-gapless semiconductor CoMnFeSi and CoFeCrAl are discussed considering the atomic ordering. Further, the case both X and Y are Mn and Z is Ga, Mn_3Ga, is also discussed with the interfacial thermal diffusion probed by XMCD.

10.1 Introduction

Since the discovery of magneto-optical techniques using synchrotron radiation, the electronic and magnetic states in solids are widely investigated for functional magnetic materials. Several techniques have been developed for spectroscopy, diffraction, scattering, and microscopy including space and time resolutions. Among them, the most distinctive features for magnetic investigations using synchrotron radiation are the element-specific studies for magnetic materials, which unveil the intrinsic electronic and magnetic properties in the materials. The magneto-optical Kerr effect (MOKE) is well known referred to as 'Faraday effect' which originates

J. Okabayashi (✉)
Research Center for Spectrochemistry, The University of Tokyo, Tokyo, Japan
e-mail: jun@chem.s.utokyo.ac.jp

K. Z. Suzuki · S. Mizukami
WPI-Advanced Institute for Materials Research, Tohoku University, Sendai, Japan

Center for Spintronics Research Network (CSRN), Tohoku University and Center for Science and Innovation in Spintronics (CSIS), Tohoku University, Sendai, Japan

K. Yamanouchi et al. (eds.), *Progress in Photon Science*, Springer Series in Chemical Physics 125, https://doi.org/10.1007/978-3-030-77646-6_10

from the difference in absorption coefficients between right- and left-circularly polarized lights, leading to magnetic circular dichroism (MCD) [1]. For the incident beam, the ultra-violet region has been utilized with optical polarizer. Since the initial and final states are not decomposed in the visible regions, magnetic excitations from localized core levels can be a direct probe detecting the occupied and unoccupied states in electronic and magnetic states. By using synchrotron radiation beams, in particular, circularly polarized beams in the soft- and hard-x-ray regions, magneto-optical techniques with MCD using circularly polarized x-rays have been extensively developed, referred as x-ray MCD (XMCD) techniques [2]. Therefore, the difference in x-ray absorption spectroscopy (XAS) between different polarized beams is defined as XMCD.

In the x-ray absorption measurements, there are several detection types as transmission, electron yield, and fluorescent yield mode. During the absorption processes, transmission geometry is the most straightforward method for detecting the absorption signals. However, since most of interesting materials are bulk or thin films on the substrate or interfacial hetero-structures, transmission mode cannot be applicable without fabricating some devices. Collecting total electrons emitted from the samples through the excitation by incident beams yields to the absorption processes, which is most utilized for XMCD as a conventional technique. However, the electron yield mode also has a disadvantage as a surface sensitive measurement beneath 5 nm from the surfaces. Electron yield γ is expressed as (10.1) by using absorption coefficient μ [m^{-1}] and depth L;

$$\gamma \propto 1 - e^{-\mu L} \approx \mu L \quad (1/\mu \gg L). \tag{10.1}$$

Because of the mean free path $1/\mu$ of incident x-rays of approximately 100 nm, the probing depth is estimated as $L \lesssim 5$ nm. In this condition, the electron yield is approximately proportional to absorption coefficient. On the other hand, the fluorescence mode is also applicable for XAS. Conventional fluorescent detector of silicon drift detector is available recently. Although it has a great advantage as bulk-sensitive, the self-absorption processes also occur, which cannot be distinguished from intrinsic signals and is necessary to correct the intensities.

After Schütz et al. experimentally observed the XMCD of the Fe K-edge in 1987 [3], Chen et al. succeeded in the measurements of XMCD of Ni L edges in soft X-rays [4]. Selection rules for optical absorption permit a transition in case of the difference of angular quantum numbers l as $\Delta l = \pm 1$, which corresponds to an excitation from p to d states in transition-metal (TM) compounds. For 3d TMs, the L-edge absorption energies are located at the soft-X-ray regions. Magneto-optical sum rules, proposed by Carra and Thole in 1992, enabled quantitative estimations of spin and orbital magnetic moments [5, 6] and widely utilized for the analysis of XMCD. In 1995, Chen et al. proposed conventional methods for the estimations of spin and orbital magnetic moments from sum rules using Fe and Co films in transmission set up [7]. XMCD and its spectral analysis using sum rules became one of the standard techniques to deduce element-specific magnetic properties. During the recent decade, XMCD techniques have been continuously extended and combined

with other techniques, which led to the development of XMCD microscopy [8] and time-resolved measurements [9] and external-field induced XMCD [10].

[Magneto-optical sum rules]

As XMCD analysis methods, magneto-optical sum rules for spin and orbital magnetic moments were established. Here, the principles of XMCD and their sum rules are discussed.

First, the dipole transition by circular polarized beams is considered. For the beams propagating along *z*-direction, circular polarized electric fields are defined as $E = E_x(100) \pm iE_y(010)$ for right and left hand side, respectively. Then, dipole moments are written as $er \cdot E = \mathrm{e}(\mathrm{x}E_x \pm iyE_y)$. *Second*, in hydrogen atom model as a most simple case, the wave functions are represented using quantum number sets (n, l, m) as $\Psi_{nlm} = (\frac{1}{\sqrt{2}})R_{nl}(r)Y_{lm}(\theta)e^{im\phi}$ by using polar coordinates [11]. In the case of dipole transition from ground states sets to other sets, the finite transition matrix elements are limited only in following four cases [12, 13];

$$(x+iy)^{n',l+1,m+1}_{n,l,m} = \sqrt{\frac{(l+m+2)(l+m+1)}{(2l+3)(2l+1)}}R^{n',l+1}_{n,l} \tag{10.2}$$

$$(x-iy)^{n',l+1,m-1}_{n,l,m} = -\sqrt{\frac{(l-m+2)(l-m+1)}{(2l+3)(2l+1)}}R^{n',l+1}_{n,l} \tag{10.3}$$

$$(x+iy)^{n',l-1,m+1}_{n,l,m} = -\sqrt{\frac{(l-m)(l-m-1)}{(2l+1)(2l-1)}}R^{n',l-1}_{n,l} \tag{10.4}$$

$$(x-iy)^{n',l-1,m-1}_{n,l,m} = \sqrt{\frac{(l+m)(l+m-1)}{(2l+1)(2l-1)}}R^{n',l-1}_{n,l}. \tag{10.5}$$

Here, the radial function is defined as

$$R^{n',l'}_{n,l} = \int R_{n'l'}(r)R_{nl}(r)r^3\mathrm{d}r.$$

Since the XMCD signals are produced as the difference between circular polarized transitions, the values of $D = (2)^2 - (3)^2$ and $(4)^2 - (5)^2$, corresponding to circular dichroism, are necessary for XMCD intensities because the square of transition matrix elements is proportional to transition probability. The former case increases l and when m is a positive value, the XMCD signal appear as positive intensity. On the other hand, the latter case, the transition with decreasing l occurs and the relation between m and XMCD signal is opposite. By using the total angular momentum representation j, the former and latter cases are written as $j = l \pm s$. Here, since the m is not controlled in the spin exchange splitting even in the ferromagnetic materials, the m is modified through the spin–orbit coupling which is the origin for arising the finite XMCD signals.

For 3*d* TM compounds, the transitions from spin–orbit split $2p_{3/2}$ and $2p_{1/2}$ to 3*d* states are considered. In these cases, the values of *D* are calculated using above relations for both edges, respectively,

$$D = \pm\frac{2m}{2l+1}\left(R_{n,l}^{n',l+1}\right)^2. \tag{10.6}$$

In this notation, the dipole transition depends on *m*.

Third, the 2*p*-3*d* transition through the non-polarized beam is considered. In this case, *m* should not be included in the transitions by non-polarized beam. The dipole transition matrix elements by non-polarized excitation becomes a finite value only in following conditions,

$$z_{n,l,m}^{n',l+1,m} = \sqrt{\frac{(l+1)^2 - m^2}{(2l+3)(2l+1)}}\,R_{n,l}^{n',l+1} \tag{10.7}$$

$$z_{n,l,m}^{n',l-1,m} = \sqrt{\frac{l^2 - m^2}{(2l+3)(2l+1)}}\,R_{n,l}^{n',l-1}. \tag{10.8}$$

In the case of 2*p*3*d* transition with increasing *l*, the transition probability can be described as an absorption intensity $I = \frac{((2)^2+(3)^2)}{2} + (7)^2$;

$$I = \frac{l+1}{2l+1}\left(R_{n,l}^{n',l-1}\right)^2 n_{\mathrm{h}},$$

Here, n_{h} is the hole number in 3*d* states. Using (10.6),

$$\frac{D}{I} = \frac{2m(l+1)}{n_{\mathrm{h}}}.$$

Since the average value of *m* is defined as an orbital angular momentum $\langle L_z\rangle$, the following notation is deduced,

$$\langle L_z\rangle = \frac{n_{\mathrm{h}} D}{2I(l+1)}.$$

Finally, in general case of dipole transition, the sum rule for orbital angular momentum is represented as follows,

$$\frac{\int(\mu_+ - \mu_-)\mathrm{d}\omega}{\int(\mu_+ + \mu_- + \mu_0)\mathrm{d}\omega} = \frac{l'\left(l'+1\right) - l(l+1) + 2}{2l'(l'+1)}\left(\frac{\langle L_z\rangle}{n_{\mathrm{h}}}\right). \tag{10.9}$$

Here, l' is initial occupied core level, l is unoccupied final states. Left-side term corresponds to D/I. In the special case of $l' = l + 1$, conventional orbital sum rule is deduced.

Next, the spin sum rule is discussed. The values of $D_{j\pm}$ are defined as spin–orbit split states. Due to the existence of magnetic dipole term $\langle T_z \rangle$, the spin sum rule becomes a complicated formulation not only for spin angular momentum $\langle S \rangle$ but also including $\langle T_z \rangle$. A general formula is established as follows,

$$\frac{D_{j+} - \left\{\frac{l+1}{l}\right\} D_{j-}}{2l} = \frac{l'\left(l'+1\right) - l(l+1) - 2}{3l}\left(\frac{S_z}{n_\mathrm{h}}\right) + \frac{l'\left(l'+1\right)\left\{l'\left(l'+1\right) + 2l(l+1) + 4\right\} - 3(l-1)^2(l+2)^2}{6l'l(l'+1)}\left(\frac{T_z}{n_\mathrm{h}}\right). \quad (10.10)$$

Here, $D_{j\pm}$ represent the excitation of spin–orbit coupled core levels. In the case of $2p3d$ transition, the notation is simply written as

$$\frac{D_{3/2} - 2D_{1/2}}{2} = \frac{2}{3n_\mathrm{h}}(\langle S \rangle + 7\langle T_z \rangle). \quad (10.11)$$

The $\langle T_z \rangle$ term appears corresponding to the low symmetry circumstance around TM ions. Usually, this term might be ignored but it appears at the interface and strained cases. In the cases of cubic-symmetry Heusler alloy compounds, this term might be negligible for the estimation of spin magnetic moments.

By summarizing the TM L-edge absorptions by circular polarized beams, transition probabilities are schematically shown in Fig. 10.1. Depending on circular polarization q $= \pm 1$, XMCD intensities arise at L_3 and L_2 edges.

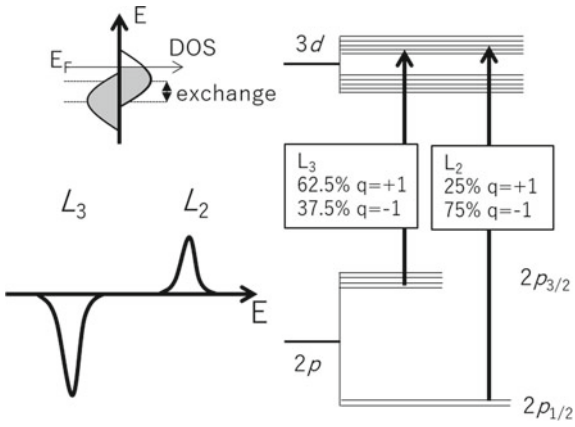

Fig. 10.1 Schematic illustration of XMCD. The spin-up and -down band structures are drawn with exchange splitting. Transition-metal L-edge excitation by different circular polarization q $= \pm 1$ from $2p$ to $3d$ states. Corresponding XMCD line shape is also displayed in L-edge [13].

10.2 Heusler Alloy Compounds

In the research fields of spintronics which are utilized in applications such as magneto-resistive random access memory (MRAM), an efficient spin current transfer without energy loss is an urgent issue in the material designs. For this motivation, there are many researches focusing on the material development of high spin polarization. As one of the final goals, 100% fully spin-polarized case is necessary. In the electronic band structure, while only up spin states contribute to the conduction electron, the other has an energy gap, which is defined as a "half metal" material. Therefore, it is required possessing the properties of half-metallicity, room temperature ferromagnetism, and good lattice matching to form abrupt interfaces with major substrates and insulating energy barrier materials, which is applicable for MRAM technologies.

Considering these demands, Heusler alloys and their related family materials are categorized in the best materials. Heusler alloys are ternary alloys originally discovered by Heusler [14]. He demonstrated the ferromagnetic property including nonmagnetic atoms in Cu_2MnSn. The original composition is defined as X_2YZ, where X and Y are transition-metal elements, and Z consists of a semiconductor or nonmagnetic atom. The unit cell of the ideal crystalline structure ($L2_1$ phase) consists of four face-centered cubic sublattices (space-group Fm-$3m$, No. 225). Stacked structures of $L2_1$ phase consist of X layer and by YZ layer in face-centered cubic structures as shown in Fig. 10.2. When the Y and Z atoms exchange their sites (Y–Z disorder) and eventually occupy their sites at random, the alloy transforms into the $B2$ phase. By increasing the disorder, the magnetic properties depart further from the half-metallicity. In order to achieve giant magnetoresistance (GMR) of higher than 100% and tunnel magnetoresistance (TMR) ratio of higher than 1000% at room temperature (RT), a great deal of effort has accordingly been devoted using a Heusler alloy [15–20].

As a typical Co-based Heusler alloy using Si as a nonmagnetic semiconductor element, Co_2MnSi and partially substituted $Co_2(Fe,Mn)Si$ are thoroughly investigated. Half metallicity of these materials are studied by the point contact Andreev

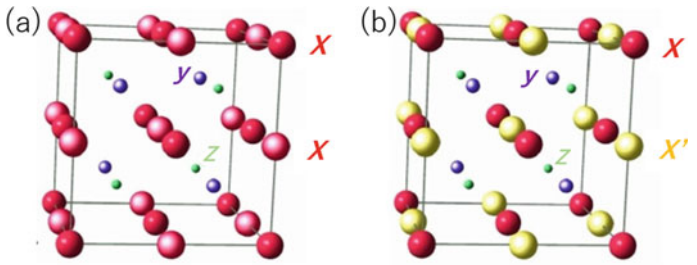

Fig. 10.2 Crystalline structures of **a** $L2_1$-type Heusler alloy X_2YZ and **b** $XX'YZ$ equatorial ordered alloy (Y-structure)

refection technique, analysis of TMR ratio using Julliere's model and guaranteed from the first-principles calculations [21, 22]. A critical subject to overcome is the large temperature dependence of spin polarization. In the case of $Co_2MnSi/MgO/Co_2MnSi$ magnetic tunnel junction, TMR is 2010% at 4.2 K, but it decreases to only 335% at 290 K [23]. It is believed as not only the interfacial atomic diffusion with MgO the insulator but also the interfacial spin fluctuation [24, 25]. Therefore, element-specific investigations near the interface regions using XMCD are strongly desired.

In order to understand the band structure of Heusler alloys, the spin-dependent densities of states (DOS) are investigated by the first-principles calculations, which is strongly related to the discussion deduced from XMCD and photoemission spectroscopy. There are many reports discussing the DOS of Co-based Heusler alloys and exhibiting half metallicity. The electronic structures of Heusler alloy are understood based on the molecular orbital picture. The hybridization between Y and Z sites split the boding and anti-bonding states. Further, hybridized states are recoupled with X layer. After filling of electron numbers, the Fermi level (E_F) is determined and mainly X sites are located in the E_F with half metal states qualitatively. This scenario is described in Fig. 10.3. In particular, the recent report of the band structure calculation by Nawa and Miura suggests the importance of intra-Coulomb interaction in Heusler alloy Co_2MnSi, especially in Mn site [26]. They drew the band diagram based on the molecular-orbital picture considering ternary elements which is developed by I. Galanakis [27]. The E_F is located in the Co 3*d* states and Coulomb interaction in the Mn site shift the level to maintain the half metallicity. Further, total valence electron number Z in X_2YZ obeys a Slater-Pauling curve with the relation of magnetization

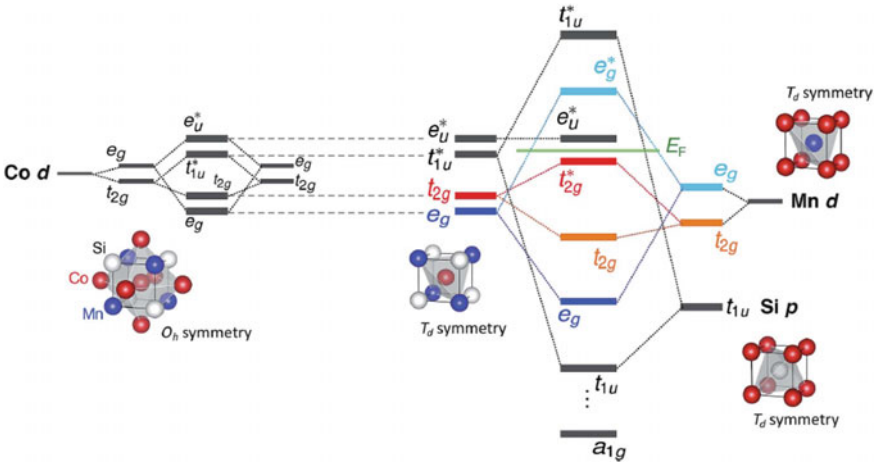

Fig. 10.3 Schematic diagram of Co_2MnSi based on molecular orbital picture. Left side is Co 3*d* states hybridized within the layer in O_h symmetry. Right side is the hybridization between Mn 3*d* and Si 3*p* valence states in T_d symmetry within the layer. Total electronic structure is also shown with the Fermi level [26]

M; $M = Z - 24$, which is established as a guideline designing the Heusler alloy compounds [27].

[Related Heusler alloy compounds]

Other Heusler alloy family is also introduced. Half-Heusler alloy compounds are defined as XYZ, where one of the X site forms a vacancy site. NiMnSb alloy was discovered in 1983 [28]. In the full-Heusler type compositions, the substitution of Y site is also effective to enhance the TMR ratio through the tuning of the DOS at E_F. Other candidate is the quaternary alloys; $XX'YZ$ with different X and X' elements (space-group F-43m, No. 216) because of tailoring of the DOS in the vicinity of E_F. The crystal structure is defined as a LiMgPdSn prototype or Y structure. It can be conceived by the combination of two ternary Heusler alloys, such as X_2YZ and X'_2YZ. In some cases, the specific band structure is modulated as spin-gapless semiconductor (SGS), where both majority and minority bands have an energy gap at E_F. The DOS of SGS is originally derived from strict condition from that of Heusler alloys. Due to their unique band structures, SGSs have been predicted to possess interesting properties, such as (i) spin-polarized current resulting from the electrons as well as holes; (ii) high spin polarization; and (iii) tunable spin polarization by voltage varying the Fermi level.

One of the advantages of SGS corresponds to the development of ferromagnetic semiconductor research field. Most famous material (Ga,Mn)As, in which Mn ions are doped into GaAs, exhibits ferromagnetism. Required items are RT ferromagnetic ordering, compatible with semiconductor technology, and carrier controlling by external fields. There were extensive efforts for clarifying the band structures of ferromagnetic semiconductors. As shown in Fig. 10.4, the hybridized states between Mn 3d and As 4p orbitals with opposite sign of exchange coupling between them correspond to the E_F which is revealed by angle-resolved photoemission spectroscopy [29, 30]. On the other hand, the SGSs are the *ultimate cases* overcoming the issues

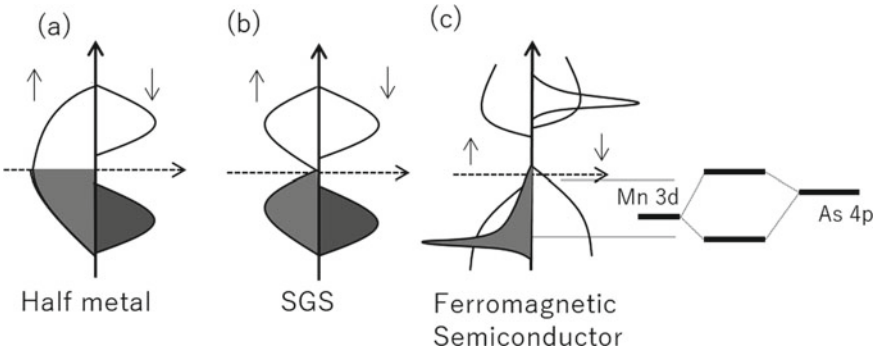

Fig. 10.4 Schematic illustrations of spin-dependent density of states of **a** half-metal, **b** spin gapless semiconductor, and **c** TM-doped ferromagnetic semiconductor (Ga,Mn)As. Schematic molecular orbital hybridization between TM 3d impurity states and host semiconductor 4p states is also illustrated

in doped ferromagnetic semiconductors because the SGSs satisfy the RT ferromagnetism and compatible with semiconductor substrate because they are composed by semiconductor Z element in the composition.

When the X and Y are Mn and Z is Ga cases, Heusler-type compounds are Mn_3Ga [31]. This material and related different composition $Mn_{3-\delta}Ga$ is well known as hard magnets which exhibit large perpendicular magnetic anisotropy (PMA). Highly ordered alloy MnGa consists of alternative Mn layer and Ga layer stacked structure, which is categorized as $L1_0$ type. With increasing Mn concentration, Ga site is substituted by Mn atoms with opposite spin direction as $D0_{22}$ type. This material is discussed in the Sect. 10.3.3 and 10.3.4.

Another aspect in topological phenomena using Heusler alloys is also interested in solid state physics as Weyl semimetals. The characteristic band structure is recognized as an appearance of Weyl points, resulting in anomalous Hall conductivity in Heusler alloy Co_2MnAl [32]. The Hall conductivity is explained as Berry curvature, which might open up new research field using Heusler alloys. Further, large thermoelectric phenomena are also demonstrated through the topological nature in Heusler alloys [33, 34].

[Aim of this study]

We investigate the element-specific magnetic and electronic structures of Heusler alloy compounds using the XMCD of 3*d* TM based Heusler alloy compounds using the *L*-edge photoexcitation from 2*p* to 3*d* states.

10.3 Results and Discussion

The element-specific magnetic and electronic structures in Heusler alloy based materials of SGS candidates are discussed for CoFeMnSi (Sect. 10.3.1), CoFeCrAl (Sect. 10.3.2). Further, in the case of both X and Y are Mn and Z is Ga, Mn_3Ga and related $Mn_{3-\delta}Ga$ are focused on the materials possessing perpendicular magnetic anisotropy (PMA) in Sect. 10.3.3. In Sect. 10.3.4, interfacial chemical reaction between $Mn_{1.5}Ga$ and TMs probed by XMCD is discussed.
[Experimental conditions for XMCD]

All experiments of XAS and XMCD system were performed using soft x-rays in the range of 50–1200 eV constructed at the BL-7A, Photon Factory, High-Energy Accelerator Research Organization (KEK) in Tsukuba, Japan [35]. For XMCD, a $\pm$ 1.2-T electromagnet has been installed at the end station. As the beam comes from the bending magnets, circularly polarized lights for XMCD are obtained using the edges from the beam center, which is adjusted by a mirror in the beam-line. The beam and magnetic-field directions are fixed to be parallel, and the sample surface normal direction is rotated for the angular-dependent XMCD. Total-electron-yield (TEY) modes are utilized for XMCD measurements.

10.3.1 Candidate for Spin-Gapless Semiconductor CoFeMnSi[1]

Dai et al. first predicted that CoFeMnSi (abbreviated as CFMS hereafter) is a half-metallic equiatomic quaternary Heusler alloys (EQHAs) from ab initio calculations and investigated the polycrystalline bulk sample [36]. The proposed Wyckoff coordinate is Co, Fe, Mn, and Si occupying the sites corresponding to *X*, *X'*, *Y*, and *Z*, respectively. Depending on the occupation of various lattice sites, three different types of *Y*-structure are possible for CFMS, i.e., types I–III [36]. The remarkable difference of CFMS is a net magnetic moment of 4 μ_B/f.u. (where f.u. represents formula unit) smaller than those for Co_2MnSi (5 μ_B/f.u.; type-I) and Co_2FeSi (6 μ_B/f.u.; type-II) and a presence of a pseudo energy band gap in the majority spin channel at the Fermi level [36, 37]. Type-III is defined as the Co site is also swapped with Fe–Mn layer. Xue et al. [38] theoretically predicted that CFMS is the spin-gapless semiconductor, although the existence of the majority spin band gap for CFMS is still under discussion from the theoretical points of view [39, 40].

Relatively high spin-polarization *P* of 64% was reported using the point contact Andreev reflection spectroscopy and nonmetallic conduction suggesting a spin-gapless semiconductor in the bulk polycrystalline CFMS samples [37], which is expected to be favorable for device applications, such as magnetic tunnel junctions. Here, the structural and magnetic properties for CFMS films grown on Cr-buffered MgO substrates are focused. This is because the use of a Cr buffer is a standard technique to obtain high-quality films with atomically flat surfaces, even though the transport properties for CFMS itself cannot be measured due to the presence of a low-resistive Cr buffer.

The sample of (001) MgO substrate/Cr(40)/CFMS(30)/Mg(0.4)/MgO(2) was prepared in the thickness of nm scales. The MgO(001) substrate was flushed thermally at 700 °C prior to the deposition process. All of the layers were deposited at RT. The Cr layer was in situ annealed at 700 °C for 1 h before the CFMS deposition in order to obtain an atomically flat Cr surface with (001) orientation. The XMCD measurements were carried out in a grazing incidence setup to the sample surface normal in order to detect the in-plane spin and orbital magnetic moments. All the measurements were performed at RT.

Figures 10.5 shows the XAS and XMCD of Mn, Fe, and Co $L_{2,3}$ edges, respectively. XAS are normalized by the photon fluxes. Clear metallic peaks are observed, which confirms that there is no mixing of oxygen atoms in the thin CFMS layer. Shoulder structures appear in the higher photon energy region of Co L_3 XAS peaks. These structures correspond to the Heusler alloys due to the Co–Co bonding states within the molecular orbital calculations [27]. The spin and orbital magnetic moments are estimated by applying the magneto-optical sum rules, and their values are estimated using the values using the sum rules, we assumed 3*d* hole numbers of 4.3, 3.4, and 2.5 for Mn, Fe, and Co, respectively, as the standard values [7]. For Mn, a

[1] This section is partly reproduced from L. Bainsla, R. Yilgin, J. Okabayashi, A. Ono, K.Z. Suzuki, and S. Mizukami, Physical Review B 96, 094,404 (2017), with the permission of APS Publishing.

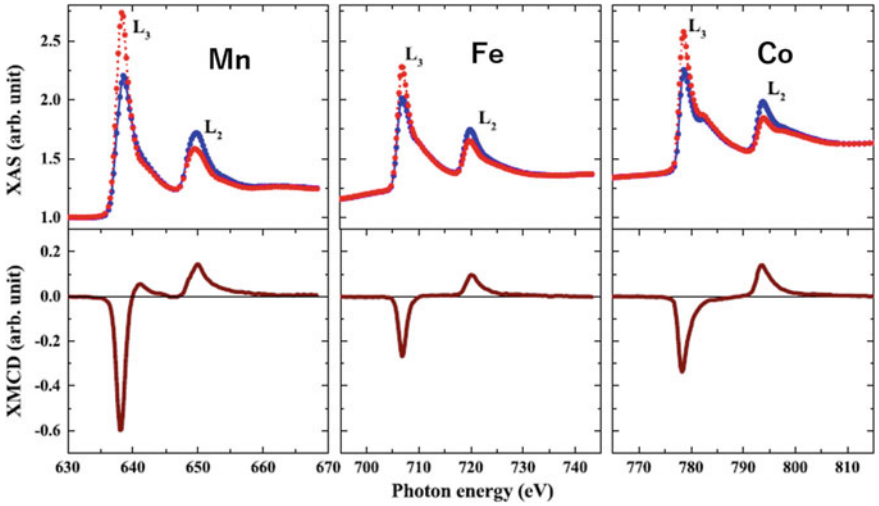

Fig. 10.5 XAS and XMCD spectra of CFMS for Mn, Fe, and Co *L*-edges. Red and blue curves correspond to photon helicities [45]

correction factor of 1.5 is applied as used previously for other Heusler alloys [41] and described in [42, 43]. The magnetic-field dependence at each transition-metal *L*3 edge was also measured, then confirmed that the magnetic fields of ± 1 T are enough to saturate the magnetization. Therefore, the spin and orbital moments are detected essentially for this alloy. The total magnetic moments evaluated by magnetization measurements are comparable with the XMCD values. The spin magnetic moments for Co, Fe, and Mn sites were 0.82, 0.77, and 2.01 μ_B, respectively, which is very close to the values reported for the bulk CFMS [41]. The obtained magnetic moment values for Fe and Co atoms in CFMS are three times smaller than those in reported bulk values. The total magnetization value obtained from XMCD is higher than the macroscopic magnetization value, which may be due to the estimation error in the Mn moment using the correction factor.

Next, we discuss the atomic disorder and its influence on the electronic structures. Dai et al. calculated the element-specific magnetic moments for the *Y* structure for CFMS as type-I ordering and for CMFS as type-II ordering [36]. In their calculations, Co had a similar magnetic moment, whereas Mn (Fe) had large magnetic moments for type-I (II) ordering, and the net values for both types were similar. Klaer et al. explained their magnetic moment value for the bulk sample by considering the Mn-Fe disorder, which was modeled by the weighted average of the magnetic moment values for type-I and type-II orderings [41]. The results obtained in this work can be explained similar to the bulk case, although we could not confirm whether our films form the *Y*-type order or not from XMCD and x-ray diffraction crystalline structure analysis. The moment value for Mn is slightly lower (∼10%), whereas the Fe moment is about 20% higher as compared to the bulk. Thus, a slightly higher Mn-Fe swapping (mixing of type-I and type-II with partially $L2_1$ and fully *B*2 orders) is expected in

the films. Considering the calculations by Klaer et al. [41], the dominant phase is type I (about $80-90\%$) with partial $L2_1$ and full $B2$ orders. According to theoretical calculations by Dai et al. [36] CFMS with type-I ordering has a pseudo gap at the Fermi level in the majority spin band and a large energy gap in the minority spin band, whereas this is not the case for type-II ordering. CFMS with type-II ordering may be the half-metallic with a smaller energy band gap in the minority spin band. This implies that the half-metallicity still remains in the presence of Mn-Fe swapping in CFMS even though Mn-Fe swapping increases the density of state at the Fermi level for the majority spin band. Feng et al. also studied the effect of various types of disorders on the electronic and magnetic properties of CFMS using the first-principles calculations, and they concluded that the half-metallicity of CFMS was broken by the appearance of Co antisites [44] and changed to type-III. In our films, the Co antisite may be negligible since the Co magnetic moment is similar to the Y structure. Therefore, the half-metallicity is expected in our films [45].

10.3.2 Candidate for Spin-Gapless Semiconductor CoFeCrAl[2]

Equiatomic quaternary Heusler alloy (EQHA) CoFeCrAl is discussed, which is a typical candidate for SGSs with a chemical formula of *XX'YZ*, where *X*, *X'*, and *Y* denote transition metal elements and *Z* represents a main group element. The crystal structure of EQHAs is a cubic LiMgPdSn or *Y*-type structure. Here, *X* is Co cite, *X'* and *Y* are positioned by Fe or Cr, and *Z* is Al cite. Basically, the Y-structure means the swap of the sites of Co and Fe within the layer and the swap between Cr and Al within the other layer. Other cases are swapping between Fe and Cr through the interlayers. Further randomness is full swapping cases. To realize SGSs, it is of vital importance to characterize the chemical orderings of EQHAs and understand their effect on both the gapless state and half-metallic gap. Xu et al. were the first to theoretically suggest that several EQHAs, including CoFeCrAl [38]. Subsequently, Ozdogan et al. theoretically studied the electronic structure of 60 EQHAs and confirmed that CoFeCrAl becomes an SGS [39]. Many experimental and theoretical studies on CoFeCrAl have since been reported [46–50]. CoFeCrAl epitaxial thin films grown on MgO substrates using a sputtering deposition technique were prepared [47, 48], which exhibit the $L2_1$ chemical order, and measured matgnetic moment of $2.0\,\mu_B$/f.u., $T\mathrm{c} = 390$ K, a semimetal-like carrier number density of 1.2×10^{18} cm^{-3}, and $P = 68\%$ [47]. Considering previous studies, the element-specific characteristics for CFCA is strongly demanded.

All samples were deposited on MgO(100) single-crystal substrates using a magnetron sputtering technique. The MTJ staking structure was

[2] This section is partly reproduced from T. Tsuchiya, T. Roy, K. Elphick, J. Okabayashi, L. Bainsla, T. Ichinose, K.Z. Suzuki, M. Tsujikawa, M. Shirai, A. Hirohata, and S. Mizukami, Physical Review Materials 3, 084,403 (2019), with the permission of APS Publishing.

substrate/Cr(40)/CoFeCrAl(30)/Mg(0.4)/MgO(2)/CoFe(5)/IrMn(10)/Ta(3)/Ru(5) (thickness is in nanometers). Before the deposition the surfaces of the substrates were cleaned by flushing at 700 °C in the chamber. All layers were deposited at RT. The Cr buffer layer was annealed in situ at 700 °C for 1 h to obtain a flat surface with (001) orientation. The CoFeCrAl layer was deposited on the substrate using an alloy target, with the film composition of $Co_{25.5}Fe_{23.1}Cr_{28.1}Al_{23.3}$ (at.%) determined using an inductively coupled plasma mass spectrometer. The samples of substrate/Cr(40)/CoFeCrAl(30)/Mg(0.4)/MgO(2) were prepared. An insight into the electronic state near the interface of MgO and CoFeCrAl via the XMCD results with the aid of ab initio calculations that take account of possible chemical disorders is obtained.

Figures 10.6 shows the XAS and XMCD spectra, respectively, of Cr, Fe, and Co $L_{2,3}$-edges with different photon helicity for the sample annealed at 700 °C. Clear metallic peaks can be observed, confirming that there is no mixing of oxygen atoms. Shoulder structures appear in the higher-photon-energy region of the Co $L_{2,3}$-edge XAS peaks. These originate from the Co–Co bonding states in Heusler alloy structures with high degree of chemical order. No finite XMCD signals can be observed at the Cr L-edges. The spin and orbital magnetic moments were estimated by applying the magneto-optical sum rules. The magnetic moments given by summing both spin and orbital components of each element are estimated to be 1.14 and 0.52 μ_B/atom for Fe and Co, respectively. The total magnetic moment m is 1.66 μ_B/atom, which

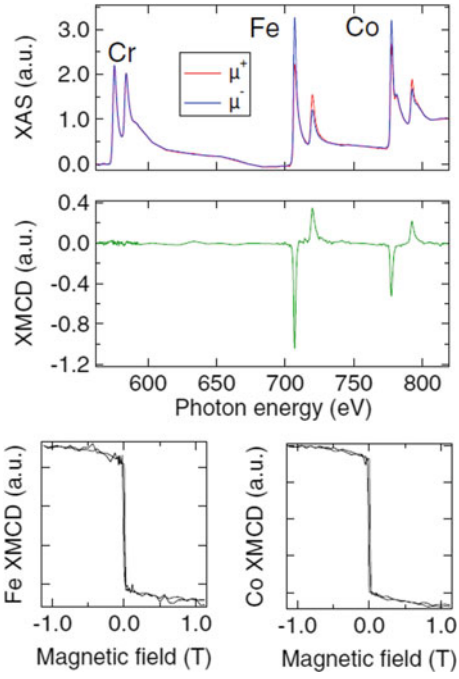

Fig. 10.6 XAS and XMCD spectra of CFCA for Cr, Fe, and Co L-edges. Red and blue curves correspond to photon helicities. Magnetic field dependence at Fe and Co L_3-edges is also shown [52]

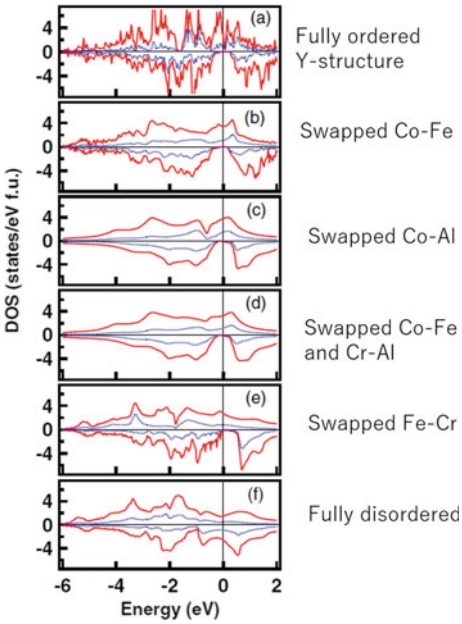

Fig. 10.7 DOS of CFCA calculated from first-principles calculation. **a** Full ordered Y structure, **b** swapped case between Co and Fe within the layer, **c** swapped case between Cr and Al within the layer, **d** swapped case Co and Fe as well as Cr and Al, **e** swapped case between Fe and Cr through interlayer, and **f** fully disordered case of Co and Cr [52]

is similar to the magnetization value of ∼1.9 μ_B/atom and the theoretical value of 2.0 μ_B/atom for *Y*-ordered CoFeCrAl. Interestingly, the XMCD results confirmed that the net magnetic moment of Co seems to be ferromagnetically coupled to that of Fe for the samples in this study. This is dissimilar to the antiferromagnetic arrangement between them that has previously been predicted for the *Y*-ordered case [49]. This finding is confirmed by the element-specific magnetic hysteresis for Fe and Co *L*-edges.

The theoretical data for the spin-resolved DOS profiles for CoFeCrAl with various chemical orderings are shown in Fig. 10.7. The lattice parameter of CoFeCrAl was fixed to 0.575 nm in these calculations. The six cases of the chemical ordering and/or disordering considered here are as follows: (i) the full ordering [*Y*-structure], (ii) the full random swapping of Co and Fe [$L2_1$ structure], (iii) the full random swapping of Cr and Al [$L2_1$], (iv) the full random swapping of Co and Fe as well as that of Cr and Al [*B*2], (v) the full random swapping of Fe and Cr [*XA*] and (vi) the full random swapping of Co and Cr [*XA*]. In cases (i)–(v), the total magnetic moment *m* is very close to 2.00 μ_B/f.u, which is consistent with the predictions given by the Slater-Pauling-like rule observed in Heusler alloys with half metallic gaps. The half-metallic gap structures in the minority spin states survive in cases (i)–(v), as seen in Fig. 10.7. However, in some cases, finite DOS appear at around the Fermi level in the gap by the disorders, meaning that the material is no longer a half-metal in a strict sense. In the case of (vi), the total magnetic moment is 3.062 μ_B/f.u., which is not consistent with the predictions given by the Slater-Pauling-like rule observed in Heusler alloys because the finite DOS appear at around the Fermi level in the gap. In

case (i) (the ordered *Y* structure), the magnetic moment associated with the Fe atom, − 0.703 μ_B/atom, is antiparallel to that of the Co and Cr atoms (1.066 μ_B/atom and 1.71 μ_B/atom, respectively). Hence, there is an overall ferrimagnetic ground state, which is in good agreement with the literature [49]. In case (ii) (Cr-Al disorder), the Fe atom, − 0.227 μ_B/atom, is antiferromagnetically coupled to both the Co and Cr atoms (0.889 μ_B/atom and 1.393 μ_B/atom, respectively). Additionally, we observe a similar kind of magnetic configuration in case (iii) (Co-Fe disorder), i.e., the Fe atom has a magnetic moment alignment opposite to that of the Cr and Co atoms, and in case (iv), both of the above disorders (Co-Fe and Cr-Al) are simultaneously present in the system. Thus, none of these cases reproduced the parallel arrangement of the magnetic moment of Fe and Co observed in XMCD. In contrast, case (v) (disorder between Fe–Cr) qualitatively reproduced the abovementioned XMCD results. The respective net moments of Fe and Co are 1.488 and 0.814 μ_B/atom, respectively, and have a parallel configuration, whereas Cr exhibits negligible net moment. The magnetic moments of Fe and Cr atoms at sites *X* (*Y*) and *Y* (*X*) are 0.268 (2.708) μ_B/atom and 1.318 (−1.682) μ_B/atom, respectively. That is, Cr has two opposite magnetic moments at different sites that tend to cancel each other out. Here, the separation between the Cr at site *X* and the Cr at site *Y* is around 0.249 nm, which is very much comparable to the separation of 0.248 nm in its bulk configuration. This may be why the antiferromagnetic coupling between two nonequivalent Cr atoms as that of its bulk configuration. In case (vi) (disorder between Co-Cr), the calculated magnetic moments also qualitatively reproduced the abovementioned XMCD results, which means Co and Fe have a parallel configuration and Cr exhibits negligible net moment. However, the magnetic moments are much larger than that for the other cases, which are quantitatively inconsistent with the magnetization measurements and XMCD results.

From the viewpoint of the formation energy, the *Y*-order state is the most stable and the Fe–Cr disorder state is unstable. Note that all these calculations result in a ground state for the bulk, whereas the experiments were conducted on films at RT. Thus, the origin of the formation of the energetically unfavorable Fe–Cr disorder can be explained as follows. Our CoFeCrAl films were deposited on the Cr buffer at RT and the in-situ annealing was done to promote the chemical ordering. This fabrication technique is one of the conventional ways to obtain the ordered alloy films with the atomically flat surface [50]. Note that this process is rather different from that in case of the well-ordered CoFeCrAl films, which was obtained at the high deposition temperature [47]. Generally, sputter deposited films at RT tend to have the disordered structure which is far from the thermal equilibrium state, similar to a rapid-cooling state. Thus, various disordered states, which are energetically higher than *Y* state, can be easily obtained. The in situ post annealing promotes the chemical ordering, so that the films have the Fe–Cr disordered state rather than Co-Cr disordered states. While, the temperature may not be enough to obtain $L2_1$ or *Y* state. Therefore, the higher temperature annealing may be one of the effective ways to obtain the ordered phase, which also requires thermally stable buffer layers to avoid significant atomic mixing. Another strategy to prevent the disorder is to partially substitute Al cation

sites by Ga. According to the bulk experiments of similar system Co_2(Cr-Fe)(Ga-Al) [51], Co_2CrFeGa system prevented to form the disorders.

10.3.3 Perpendicular Magnetic Anisotropy in $Mn_{3-\delta}Ga$[3]

Perpendicular magnetic anisotropy (PMA) is desired for the development of high-density magnetic storage technologies. Thermal stability of ultrahigh density magnetic devices is required to overcome the superparamagnetic limit [53]. Recently, research interests using PMA films have focused on not only magnetic tunnel junctions toward the realization of spin-transfer switching magneto-resistive random-access memories but also antiferromagnetic or ferrimagnetic devices [54, 55]. To design PMA materials, heavy-metal elements that possess large spin–orbit coupling are often utilized through the interplay between the spins in 3*d* transition-metals (TMs) and 4*d* or 5*d* TMs [56]. The design of PMA materials without using the heavy-metal elements is an important subject in future spintronics researches. Recent progress has focused on the interfacial PMA in Fe/MgO [57–59]. However, a high PMA of over the order of MJ/m^3 with a large coercive field is needed to maintain the magnetic directions during device operation. Therefore, the materials using high PMA constants and without using heavy-metal atoms are strongly desired.

Mn-Ga binary alloys are a candidate that could overcome these issues. $Mn_{3-\delta}Ga$ alloys satisfy the conditions of high spin polarization, low saturation magnetization, and low magnetic damping constants [60–62]. Tetragonal $Mn_{3-\delta}Ga$ alloys are widely recognized as hard magnets, basically form the Heusler alloy composition where both *X* and *Y* are Mn atoms and *Z* is Ga in X_2YZ. They exhibit high PMA, ferromagnetic, or ferrimagnetic properties depending on the Mn composition [61]. Two kinds of Mn sites, which couple antiferromagnetically, consist of $Mn_{3-\delta}Ga$ with the $D0_{22}$-type ordering. Meanwhile, the $L1_0$-type Mn_1Ga ordered alloy possesses a single Mn site. These specific crystalline structures provide the elongated *c*-axis direction, which induces the anisotropic chemical bonding, resulting in the anisotropy of electron occupancies in TM 3*d* states and charge distribution. There are many reports investigating the electronic and magnetic structures of $Mn_{3-\delta}Ga$ alloys to clarify the origin of large PMA and coercive field [63–65]. To investigate the mechanism of PMA and large coercive fields in $Mn_{3-\delta}Ga$, site-specific magnetic properties must be investigated explicitly.

The deconvolution of each Mn site using the systematic XMCD measurements for different Mn contents in $Mn_{3-\delta}Ga$ is performed. The site-specific spin (m_s) and orbital magnetic moments (m_{orb}) with magnetic dipole term (m_T) are discussed, which corresponds to electric quadrupoles to understand the PMA microscopically.

[3] This section is partly reproduced from J. Okabayashi, Y. Miura, Y. Kota, K. Z. Suzuki, A. Sakuma, and S. Mizukami, Scientific Reports 10, 9744 (2020)., in accordance with the Creative Commons Attribution (CC BY) license.

In the case of $Mn_{3-\delta}Ga$, the difficulty in the deconvolution of two kinds of Mn sites prevents site-selected detailed investigations. Within the magneto-optical spin sum rule, the m_{orb} are expressed as proportional to q/r, where q and r represent the integral of the XAS and XMCD spectra, respectively, for both L_2 and L_3 edges [7, 66]. In the cases of two existing components, the orbital moments are not obtained from the whole integrals of spectra; by using each component r_1, r_2, q_1, and q_2, the value of $(r_1/q_1) + (r_2/q_2)$ should be the average value. The value of $(r_1 + r_2)/(q_1 + q_2)$ does not make sense as an average in the case of core-level atomic excitation, leading to the wrong value in the XMCD analysis. As a typical example, for the mixed valence compound $CoFe_2O_4$, the Fe^{3+} and Fe^{2+} sites can be deconvoluted by the ligand-field theory approximation [67]. However, the deconvolution of featureless line shapes in a metallic $Mn_{3-\delta}Ga$ case is difficult by comparison with the theoretical calculations. To detect the site-specific anti-parallel-coupled two Mn sites, systematic investigations using $Mn_{3-\delta}Ga$ of $\delta = 0$, 1, and 2 provide the information of site-specific detections.

The Mn L-edge XAS and XMCD for $L1_0$-type Mn_1Ga with a single Mn site (MnI), and $D0_{22}$-type Mn_2Ga and Mn_3Ga with two kinds of Mn sites (MnI and MnII) are shown in Fig. 10.8. The XAS were normalized to be one at the post-edges. With increasing Mn concentrations (decreasing δ), the intensities of XAS increased and the difference between μ^+ and μ^- became small, resulting in the suppression of XMCD intensities because of the increase of antiparallel components. In the case of Mn_2Ga and Mn_3Ga, the XMCD line shapes in the L_3 and L_2 edges, of slightly split and

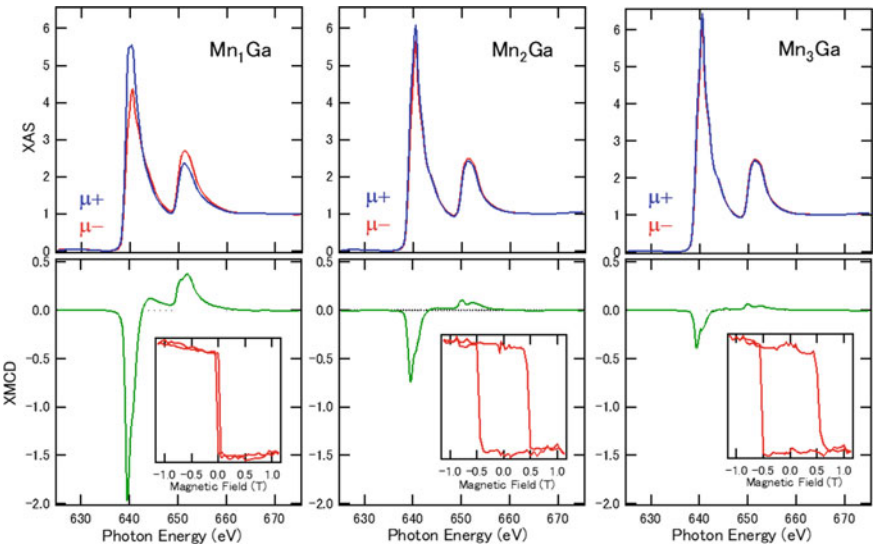

Fig. 10.8 XAS and XMCD of $Mn_{3-\delta}Ga$ for $d = 0$, 1, and 2. Spectra were measured at the normal incident setup where the incident beam and magnetic field were parallel to the sample surface normal. μ^+ and μ^- denote the absorption in different magnetic field direction. The insets show the magnetic field dependence of the hysteresis curves taken by fixed L_3-edge photon energy. All measurements were performed at RT [74].

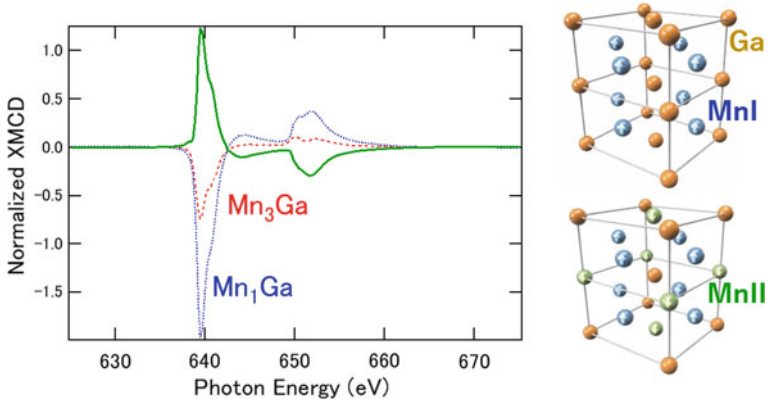

Fig. 10.9 Deconvoluted XMCD spectra of $Mn_{3-\delta}Ga$ by subtraction from Mn_1Ga. The MnI and MnII components were separated in this procedure. Illustrations of the unit-cell structures of Mn_1Ga and Mn_3Ga are also displayed [74]

doublet structures, became clear because of the increase of another MnII component with opposite sign. Furthermore, the element-specific hysteresis curves in XMCD at a fixed photon energy of Mn L_3-edge exhibit similar features with the results of the magneto-optical Kerr effects. Coercive fields (H_c) of 0.5 T were obtained for the Mn_2Ga and Mn_3Ga cases because the two kinds of Mn sites enhance the antiparallel coupling. The 3-nm-thick $Mn_{3-\delta}Ga$ samples used in the XMCD measurements were prepared by magnetron sputtering technique on MgO (001) substrates with the CoGa buffer layers. The detailed sample growth conditions are reported in [68].

To deconvolute the MnI and MnII sites in the XMCD spectra, we performed the subtraction of XMCD between Mn_1Ga and Mn_3Ga. Figure 10.9 displays the XMCD of Mn_1Ga and Mn_3Ga, and their differences after the normalization considering the Mn compositions. The XMCD signal with opposite sign was clearly detected for MnI and MnII components. As the lattice volume of $Mn_{3-\delta}Ga$ on the CoGa buffer layer remained almost unchanged with different δ, the validity of the subtraction of XMCD is warranted because the DOS for MnI is similar in all δ regions. To apply the magneto-optical sum rule for effective spin magnetic moments (m_s^{eff}) including magnetic dipole term and m_{orb}, the integrals of the XMCD line shapes are needed. Further, the integrals of XAS were also estimated for MnI and MnII, divided by the composition ratios. The electron numbers for 3*d* states of MnI and MnII were estimated from the band-structure calculations to be 5.795 and 5.833, respectively. Thus, m_s^{eff} and m_{orb} for MnI were estimated to be 2.30 and 0.163 μ_B, respectively. For MnII, 2.94 μ_B (m_s^{eff}) and 0.093 μ_B (m_{orb}) were obtained for perpendicular components with the error bars of 20% because of the ambiguities estimating spectral background. Here, we claim the validity of m_s^{eff} and m_{orb} in $Mn_{3-\delta}Ga$ deduced from XMCD. *First*, these m_{orb} values are too small to explain stabilizing the PMA because the magnetic crystalline energy $E_{MCA} \propto 1/4\alpha\xi(m_{orb}^{\perp} - m_{orb}^{\parallel})$ within the scheme of the Bruno relation [69], assuming the spin–orbit

coupling constant ξ_{Mn} of 41 meV and the band-state parameter $\alpha = 0.2$ for Mn compounds, which is estimated from the band-structure calculation. For Mn_1Ga, as the saturation magnetic field along hard axis direction was less than 1 T, the projected component ${m_{orb}}^{\parallel}$ could be deduced as $\Delta m_{orb} (= {m_{orb}}^{\perp} - {m_{orb}}^{\parallel})$ of less than 0.01 μ_B, resulting in $E_{MCA} = 1 \times 10^{-5}$ eV/atom, that is, 5.7×10^4 J/m^3 using the unit cell of MnGa. Therefore, orbital moment anisotropy cannot explain the PMA of the order of 10^6 J/m^3 in $Mn_{3-\delta}Ga$ [68]. As the electron configuration is close to the half-filled $3d^5$ case, the quenching of the orbital angular momentum occurs in principle. In $Mn_{3-\delta}Ga$, since the electron filling is not complete half-filled cases, small orbital angular momentum appears. *Second*, another origin for the large PMA is considered as the spin flipped contribution between the spin-up and -down states in the vicinity of the E_F. The magnetic dipole moment (m_T) also stabilizes the magneto-crystalline anisotropy energy (E_{MCA}) by the following equation [70, 71]:

$$E_{MCA} \sim \frac{1}{4\mu_B} \xi \Delta m_{orb} - \frac{21}{2\mu_B} \frac{\xi^2}{\Delta E_{ex}} m_T \tag{10.12}$$

where ΔE_{ex} denotes the exchange splitting of $3d$ bands. Positive values of E_{MCA} stabilize the PMA. The second term becomes dominant when proximity-driven exchange split cases, such as the $4d$ and $5d$ states, are dominant. In the case of $Mn_{3-\delta}Ga$, the Mn $3d$ states were delicate regarding the mixing of the spin-up and -down states at the E_F, which corresponds to the quadrupole formation and the band structure α values. The second term is expressed by m_T in the XMCD spin sum rule of $m_s + 7m_{Tz}$ along the out-of-plane z direction [72]. For Mn_1Ga, if m_{Tz} is negative, resulting in $Q_{zz} > 0$ in the notation of $m_{Tz} = -Q_{zz}m_s$, which exhibits the prolate shape of the spin density distribution; the second term favors PMA because of the different sign for the contribution of orbital moment anisotropy in the first term. The Q_{zz} corresponds to the quadrupole representation. Since $7m_{Tz}$ is estimated to be in the order of 0.1 μ_B from angular-dependent XMCD between surface normal and magic angle cases, Q_{zz} is less than 0.01, resulting that the orbital polarization of less than 1% contributes to stabilize PMA. In this case, the contribution of the second term in (10.12) is one order larger than the orbital term, which is essential for explaining the PMA of $Mn_{3-\delta}Ga$. *Third*, in a previous study [63], quite small Δm_{orb} and negligible m_{Tz} were reported for Mn_2Ga and Mn_3Ga. Their detailed investigation claims that Δm_{orb} of 0.02 μ_B in MnI site contributes to PMA and MnII site has the opposite sign. These are qualitatively consistent with our results. The difference might be derived from the sample growth conditions and experimental setup. Fourth, the reason why Hc in Mn_1Ga is small can be explained by the $L1_0$-type structure, due to the stacking of the Mn and Ga layers alternately, which weakened the exchange coupling between the Mn layers. *Finally*, we comment on the XMCD of the Ga L-edges shown in Fig. 10.10. Clear XMCD signals are induced with the same sign as the MnI component, suggesting that the induced moments in the Ga sites were derived from the MnI component, which was substituted by the MnII for Mn_2Ga and Mn_3Ga. In Fig. 10.10, not only L_2 and L_3-edges but also oscillation behaviors are

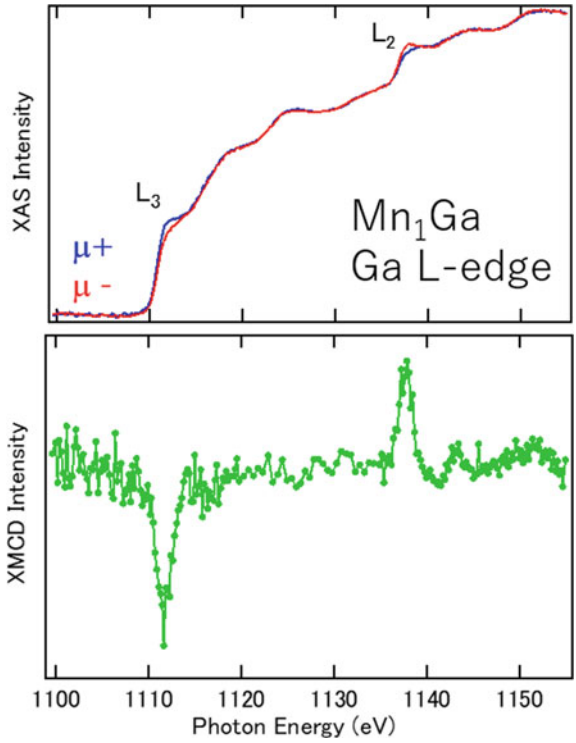

Fig. 10.10 XAS and XMCD of Mn_1Ga. Spectra were measured at the normal incident setup where the incident beam and magnetic field were parallel to the sample surface normal. μ^+ and μ^- denote the absorption in different magnetic field direction. All measurements were performed at RT

detected in XAS, which corresponds to the extended x-ray absorption fine structure and does not contribute to the magnetic signals in XMCD.

Considering the results of the XMCD, we discuss the origin of PMA in $Mn_{3-\delta}Ga$. As the orbital magnetic moments and their anisotropies are small, the contribution of the first term in (10.12) is also small, which is a unique property of Mn alloy compounds and contradicts the cases of Fe and Co compounds exhibiting PMA. Beyond Bruno's formula, the mixing of majority and minority bands in Mn 3*d* states enables the spin-flipped transition and Q_{zz}. However, comparing with the CoPd or FePt cases, where the exchange splitting was induced in the 4*d* or 5*d* states, a small ξ_{Mn} and large ΔE_{ex} in the Mn 3*d* states suppress the contribution of the second term. Large Q_{zz} values were brought by the crystalline distortion accompanied by the anisotropic spin distribution, resulting in the PMA energy of $Mn_{3-\delta}Ga$ exhibiting a similar order with those in heavy-metal induced magnetic materials. Therefore, the large PMA in $Mn_{3-\delta}Ga$ originates from the specific band structure of the Mn 3*d* states, where the orbital selection rule for the electron hopping through spin-flipped $\langle yz|L_x|z^2\rangle$ provides the cigar-type spin distribution. As the spin-flipped term for PMA energy, except the orbital contributions, can be written as:

$$E_{\text{spin-flipped}} = \sum_{u\uparrow,o\downarrow} \frac{\xi^2}{\Delta E_{\text{ex}}} \left[\langle u \uparrow | L_x^2 | o \downarrow \rangle - \langle u \uparrow | L_z^2 | o \downarrow \rangle \right]. \tag{10.13}$$

The difference between the ${L_x}^2$ and ${L_z}^2$ terms through the spin-flipped transitions between the occupied (o) to unoccupied (u) states is significant for the gain of the PMA energy. The matrix elements of $\langle yz\uparrow | L_x | z^2\downarrow \rangle$ were enhanced in the spin-flipped transition between yz and z^2, and those of $\langle yz\downarrow | L_z | z^2\downarrow \rangle$ were enhanced in the spin-conserved case between xy and $x^2 - y^2$ [73]. These transitions favor the magnetic dipole moments of prolate shapes ($\langle Q_{zz} \rangle = \langle 3{L_z}^2 - L^2 \rangle > 0$) described by the Mn $3d$ each orbital angular momenta. We emphasize that the signs of Δm_{orb} and Q_{zz} are opposite, which is essential to stabilize the PMA by the contribution of the second term in (10.12). The PMA energy of FePt exhibits around MJ/m^3 and the contribution of the second term in Pt is four times larger than the Fe orbital anisotropy energy. Therefore, MnGa has a specific band structure by crystalline anisotropy elongated to the c-axis and intra-Coulomb interaction in Mn sites to enhance the PMA without using heavy-metal atoms.

In summary, the contribution of the orbital moment anisotropy in Mn_3Ga is small and that of the mixing between the Mn $3d$ up and down states is significant for PMA, resulting in the spin-flipped process through the electron hopping between finite unforbidden orbital symmetries in the $3d$ states through the quadratic contribution. Composition dependence reveals that the orbital magnetic moments of the two antiparallel-coupled components in Mn sites were too small to explain the PMA. These results suggest that the quadrupole-like spin-flipped states through the anisotropic $L1_0$ and $D0_{22}$ crystalline symmetries are originated to the PMA in $Mn_{3-\delta}Ga$. The present study provides a promising strategy to investigate quadrupoles in antiferromagnetic or ferromagnetic materials with PMA.

10.3.4 Interfacial Exchange Coupling Between Transition Metals and $Mn_{3-\delta}Ga$[4]

As promising spintronics materials, tetragonal $L1_0$-type MnGa and $D0_{22}$-type Mn_3Ga alloys and their mixed alloy $Mn_{3-\delta}Ga$ have been extensively investigated and discussed in the Sect. 10.3.3. In order to understand the interfacial magnetic properties of multilayered structures between $Mn_{3-\delta}Ga$ and TMs, thermal and chemical diffusions at the interfaces are quite important for use in the MRAM devices using magnetic tunnel junctions. The Co substitution into $Mn_{3-\delta}Ga$ products such as Mn_2CoGa [75, 76] and the creation of magnetic tunnel junctions for TMR using Mn_3Ga/MgO/Mn_3Ga stacks of over 600% and $L1_0$-type MnGa/MgO/MnGa with an

[4] This section is partly reproduced from J. Okabayashi, K. Z. Suzuki, and S. Mizukami, Journal of Magnetism and Magnetic Materials 460, 418 (2018), in accordance with the Elsevier Science Direct.

epitaxial strain was also predicted [68, 77, 78]. Since the case of MTJs the interfaces arise inevitably between MnGa and TMs, the interfacial magnetism and the annealing effect have to be clarified explicitly to enhance the TMR characteristics.

Using the advantage that $Mn_{3-\delta}Ga$ is a hard magnetic film, the deposition of other ferromagnetic materials on $Mn_{3-\delta}Ga$ layers can be used to induce perpendicular magnetization through exchange interactions [79–83]. Ultra-thin $Fe_{1-x}Co_x$ layers deposited on $Mn_{3-\delta}Ga$ couple ferromagnetically or antiferromagnetically, depending on their compositions [82]. Antiferromagnetic coupling has been demonstrated in high-Co-concentration regions, while low-Co-concentration regions have been shown to exhibit ferromagnetic coupling. In particular, TMR ratios higher than those in as-grown samples have been found to appear after annealing at 350 °C in order to maintain the highly crystallized body-centered-cubic structures of FeCo alloys [82]. Therefore, the studies of interfacial magnetism depending on annealing temperature resolving into each element are necessary for Fe/MnGa, Co/MnGa, and Cr/MnGa cases by using XMCD for 3d TM *L*-edges and their element-specific hysteresis curves for unveiling the interfacial magnetic properties. In this sub-section, XMCD was employed to investigate the element-specific magnetic properties at TMs/$Mn_{1.5}$Ga interfaces. We discuss the interfacial coupling, which may be ferromagnetic or antiferromagnetic depending on the annealing of the samples.

The samples were prepared by magnetron sputtering. The 40-nm-thick Cr buffer layers were deposited on single-crystal MgO (001) substrates at room temperature, and in situ annealing at 700 °C was performed. Subsequently, 30-nm-thick $L1_0$-type $Mn_{1.5}Ga$ layers were grown at room temperature with in situ annealing at 500 °C. Fe and Co were sputtered at room temperature to form a layer 1 nm thick and were capped with a 2-nm-thick MgO layer. A piece of an "as-grown" sample of MgO (2 nm)/TMs (1 nm)/$Mn_{1.5}Ga$ (30 nm)/Cr (40 nm)/MgO (001) was annealed at 350 °C for 10 min to prepare the "annealed" sample. The details of the employed sample preparation method were reported in [82]. The magneto-optical polar Kerr effect (MOKE) measurement was carried out with a laser wavelength of about 400 nm and the maximum magnetic field of ± 2 T. The XAS and XMCD measurement geometries were mainly set to normal incidence because of the detection for easy-axis direction in PMA.

Figure 10.11 shows the polarization dependences of the XAS and XMCD results for the Mn and Co L_{23}-edges of the Co/$Mn_{1.5}Ga$ as-grown sample. Clear metallic spectral line shapes are observable for the Co *L*-edges. The broad line shape with the shoulder structures in the XAS results for the Mn *L*-edge is quite similar to those shown in previous reports because the two kinds of Mn components overlap as discussed in the previous section [74]. The spins of Mn and Co are coupled ferromagnetically. Because of the ferrimagnetic nature of $Mn_{1.5}Ga$, the spins of the Mn sites partially cancel, and the XMCD intensity of the Mn *L*-edge is smaller than that of Co.

After the annealing, the XMCD intensities in both Mn and Co *L*-edges become small, and the signs at the L_3 and L_2 edges in Co change. By comparing these spectral line shapes with those in the as-grown case, it is evident that the XAS intensity ratios between Mn and Co are also modulated, which suggests that the Co atoms diffuse

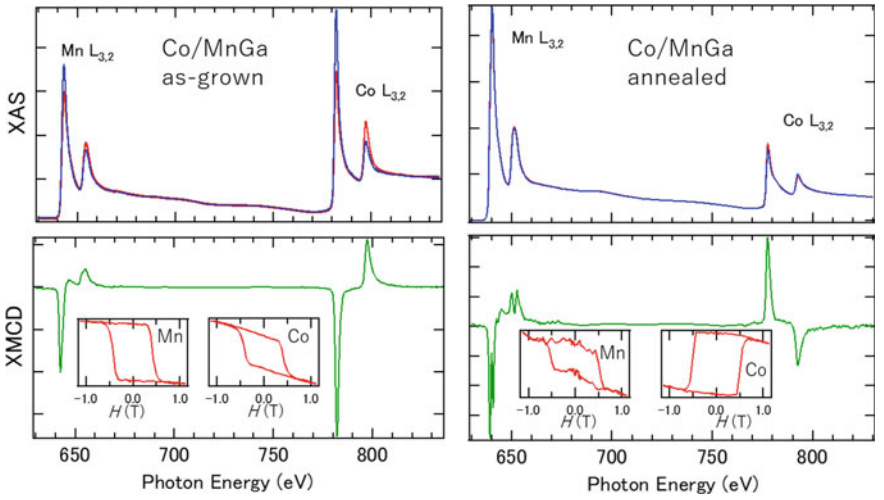

Fig. 10.11 XAS and XMCD spectra of Mn and Co *L*-edges in Co/$Mn_{1.5}$Ga. As-grown and annealed cases. Insets show the element-specific hysteresis curves taken at L_3-edges. The units of magnetic field in horizontal axis are Tesla

chemically into the MnGa layer, or vice versa, within the probing depth of beneath 5 nm from the surface with exponential detection decay. In the Mn *L*-edge XAS results, little difference between the μ^+ and μ^- XAS peaks due to the annealing process is evident, which indicates that the other antiferromagnetic Mn compounds are formed by interfacial reactions. Further, from the comparison of XAS intensities between Mn and Co, it is clear from the changes of XAS intensities by annealing. The Mn *L*-edge XMCD line shape shows two chemically shifted components, although the sign of the XMCD remains unchanged by the annealing. Generally, 1-nm-thick Co layers capped with 2-nm-thick MgO exhibit clear XMCD signals identical to those shown in the as-grown case. The fact that the differences between the μ^+ and μ^- XAS peaks of the Co *L*-edges are only slight suggests that the m_s of Co are also suppressed. Opposite XMCD signs are observed in Co, and the XMCD intensities are different from those in the as-grown case. The Co XAS line shapes exhibit small shoulder structures at the higher-energy side, which do not influence the XMCD line shapes. It might be originated from the Co-based Heusler alloy formation. Antiferromagnetic coupling between Co and $Mn_{1.5}$ Ga is consistent with the previous studies [82]. Therefore, although antiferromagnetic coupling occurs between MnGa and Co by annealing, inevitable interfacial atomic diffusion has to be also considered.

The element-specific hysteresis curves for the as-grown and annealed samples are also shown in the insets of Fig. 10.11. The photon energies at the Mn and Co L_3-edges were fixed in the normal incidence setup. In the as-grown sample, the clear hysteresis loops with a coercive field (H_c) of 0.4 T indicate PMA. In the high magnetic field regions, the intensities of Mn are saturated and become constant with almost square

while Co *L*-edge exhibits different in the high magnetic field regions with unsaturated slope. This suggests that there is no intermixing between Co and $Mn_{1.5}Ga$ at as-grown stage. In fact, the MOKE hysteresis curve also exhibits slightly increasing features in high field regions. Thus, the element-resolved hysteresis curves can clearly reveal the details of the components canted from the surface normal direction in Co.

After the annealing, interestingly, the hysteresis loops for both elements change drastically. Because of the small XMCD intensities, the statistics of the hysteresis loops are noisier than those in the as-grown cases. The characteristic features not only of the PMA, but also of the unsaturated slopes, are clearly observable for both elements and indicate the appearance of secondary phases at the interfaces with hard-axis components. The hysteresis loop of the Co *L*-edges is opposite to that of Mn, causing the XMCD signs in Co to be different. On the other hand, the slopes of the hard-axis components and the H_c values are common for both elements. For Mn, both the PMA and the in-plane components are overlapped, with the same spin direction. The PMA contributions result from the bulk $Mn_{1.5}Ga$. The slopes of Co hysteresis curves are influenced by the interfacial secondary alloy phases with anti-parallel coupling.

Next, the XAS and XMCD in the interface between Fe and $Mn_{1.5}Ga$ are shown in Fig. 10.12 in the same manner as those in Co/$Mn_{1.5}Ga$. In the case of as-grown Fe/MnGa, the line shapes of Mn XAS and XMCD is quite similar to those in Co/MnGa, which suggests that that there is no interfacial reaction at the as-grown stage. Clear XAS and XMCD in Fe *L*-edge are observed which is similar to the bulk Fe. However, hysteresis curve shown in the inset of Fig. 10.12 exhibits the

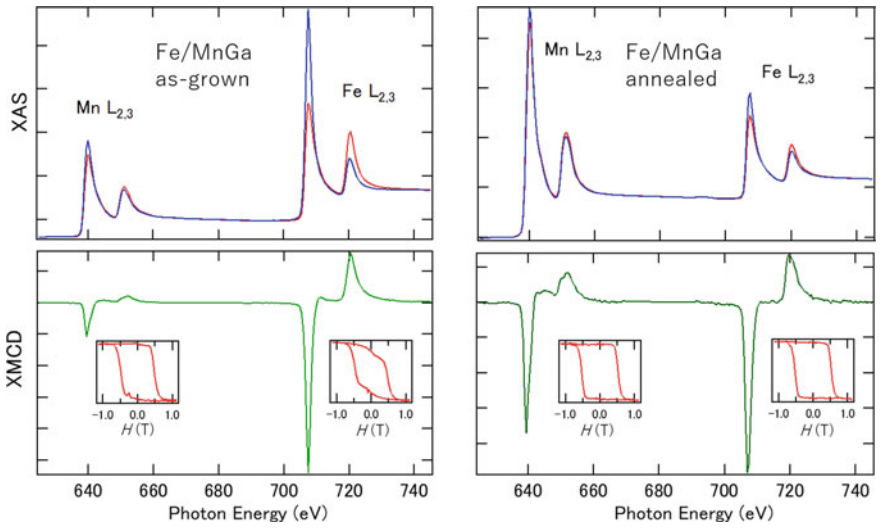

Fig. 10.12 XAS and XMCD spectra of Mn and Fe *L*-edges in Fe/$Mn_{1.5}$ Ga. As-grown and annealed cases. Insets show the element-specific hysteresis curves taken at L_3-edges. The units of magnetic field in horizontal axis are Tesla

summation of exchange coupling from MnGa and in-plane anisotropy, which is saturated at ± 0.7 T and is consistent with the MOKE results. After the annealing, the XMCD intensities of both Mn and Fe are suppressed although the line shapes remain unchanged, which is quite different from the case of Co/$Mn_{1.5}$Ga. XAS intensities also modulated. Element-specific hysteresis curves become similar, which suggests the Fe–Mn-Ga alloy formation by the annealing with the parallel coupling between Mn and Fe. Contrary to the case of Co/$Mn_{1.5}$Ga, there is no slope unsaturated at ± 1.0 T. The suppression of XMCD intensities might originate from the non-magnetic Fe–Mn-Ga alloy formation. These element-specific interfacial analyses cannot be detected by the transmission electron microscope technique because of nearly equal scattering amplitudes from Mn and Fe. Furthermore, in case of Cr/$Mn_{1.5}$Ga case, we performed similar measurements. The results shown in Fig. 10.13 clearly exhibit the no-interfacial reaction by the annealing, which argues that the interfacial reaction depends on the elements.

Considering the above results, we discuss the magnetic properties at the interfaces before and after the annealing in terms of three aspects: the exchange coupling at the interfaces, the PMA at the TMs/MgO interfaces, and the chemical reactions at the interfaces. When parallel coupling is dominant, the strong perpendicular magnetization in the TM layers is induced by exchange coupling with $Mn_{1.5}$ Ga accompanied by the large H_c values of the Fe and Co hysteresis curves. In the as-grown stages, the ratio of m_s and m_{orb} (m_{orb}/m_{spin}) was found to be 0.09 and 0.12 for Fe and Co, respectively, which is consistent with the cases of bulk Fe and Co [7]. It suggests that the interfacial reaction does not occur and PMA and large H_c is induced by

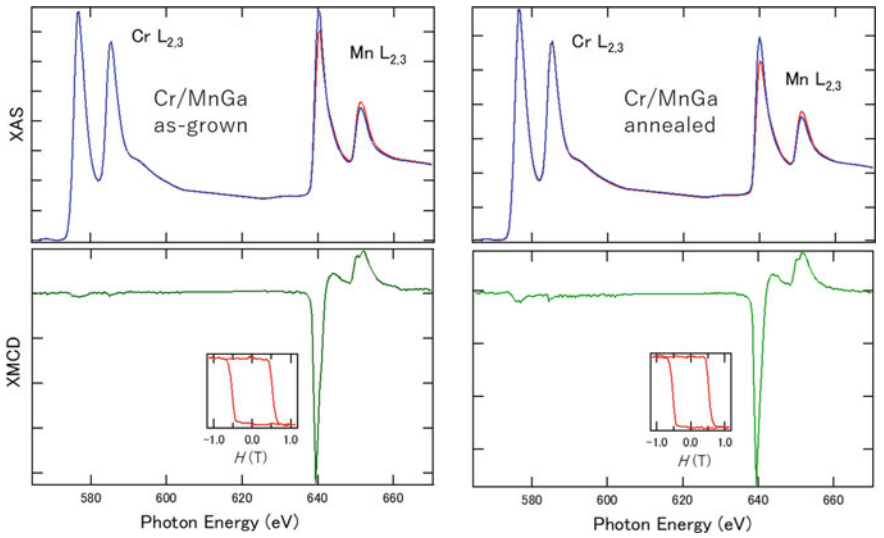

Fig. 10.13 XAS and XMCD spectra of Mn and Cr *L*-edges in Cr/$Mn_{1.5}$ Ga. As-grown and annealed cases. Insets show the element-specific hysteresis curves taken at Mn L_3-edges. The units of magnetic field in horizontal axis are Tesla

the exchange coupling from $Mn_{1.5}Ga$ layer. By annealing, anti-parallel exchange coupling becomes dominant in Co. Since the common slopes appear for both Mn and Co hysteresis curves, Co-Mn-Ga alloy formation becomes a possible candidate. Ternary-alloy phase diagram suggests the formations of Heusler-type Co_2MnGa or Mn_2CoGa [84]. In case of Co-based Heusler alloy, XAS line shapes possess the shoulder structure [27]. The line shapes of CoGa and MnCo are also different from Fig. 10.11 [68, 85]. Therefore, Mn_2CoGa-like compounds are most likely to the interfacial layer where Mn and Co are coupled antiferomagnetically. In order to confirm the alloy formation by annealing, angle dependence of XAS intensity ratios is plotted in Fig. 10.14. By tilting the angle between beam incidence and sample surface normal directions, the Co intensities are enhanced in as-grown case because the Co layer is stacked on $Mn_{1.5}Ga$. After the annealing, the ratios almost remain unchanged due to uniform alloy formation within the probing depth of XAS. On the other hand, Fe–Mn-Ga case is different. Ternary-alloy phase diagram of Fe–Mn-Ga exhibits little mixing between Fe and MnGa [86]. It suggests that the annealing promotes the interfacial coupling between Fe and MnGa, which is evident from the similar hysteresis curves after the annealing and maintaining the similar XMCD line shapes. The suppression of XMCD intensities might be derived from the non-magnetic interfacial layer formation. Furthermore, although the annealing promotes the strong chemical bonding between Fe and MgO, the exchange coupling at the Fe/$Mn_{1.5}Ga$ interface is stronger than that at the Fe/MgO. We emphasize that the interfacial secondary phases formed by annealing are not observable in a TEM image but clearly detected by the XMCD line shapes and element-specific hysteresis curves. Although the annealing process at 350 °C is necessary to obtain high quality

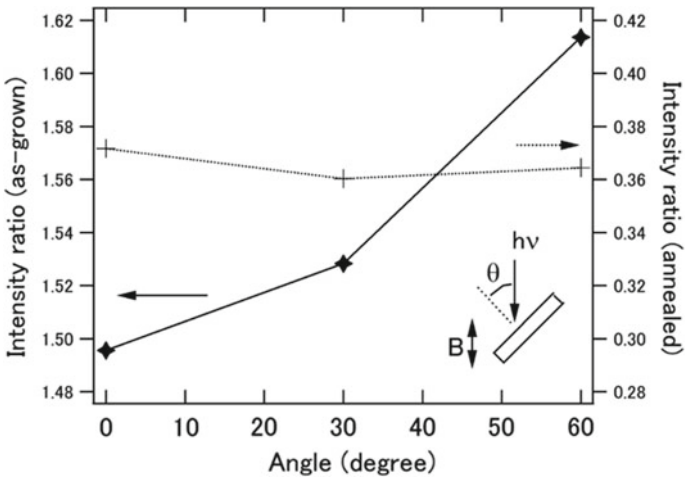

Fig. 10.14 XAS intensity ratio of Co to Mn *L*-edges depending on angle for as-grown and annealed cases in Co/$Mn_{1.5}Ga$. Inset shows the sample geometry and definition of angle. Incident beam and magnetic field directions are fixed parallel

TMs/MgO interfaces, it inevitably produces an interfacial layer at the $Mn_{1.5}Ga$/TMs boundaries, which contributes slightly to the TMR properties [77, 78].

In summary of this sub-section, by using XMCD, we found that the spins in TMs were coupled with and parallel to those in $Mn_{1.5}Ga$ under the as-grown conditions, while the post-annealing at 350 °C changed the interface magnetic coupling to antiferromagnetic in Co and ferromagnetic in Fe. The element-specific hysteresis curves at each XMCD absorption edge revealed large coercive fields in Fe and Co that obeyed the magnetic properties of $Mn_{1.5}Ga$. After the annealing, alloy formation was observed from the XAS and XMCD spectral line shapes and hysteresis curves in each absorption edge are also modulated through the interfacial alloy formation. Therefore, XMCD is a powerful tool to investigate element-specific interfacial magnetism and chemical diffusion processes [87].

10.4 Summary and Outlook in X-Ray Magnetic Spectroscopies for Heusler Alloys

Recent XMCD studies for Heusler alloys and related compounds were reviewed to clarify the element-specific electronic and magnetic states. As discussed above, the electronic structures of alloys are modulated by composition and degree of ordering, which developed novel properties such as magnetic semiconductors or SGS, PMA, antiferromagnetic or ferromagnetic ordering, topological band engineering. As the next steps of material designing using Heusler alloy based compounds, following items are necessary.

(i) The PMA properties with half-metallic properties are strongly desired without using heavy-metal elements. Recent progresses are developed by using interfacial atomic controlling with MgO for TMR device applications. The PMA at MgO/Co_2FeAl is one of the ultimate cases possessing both PMA and half-metallic properties [88, 89]. Interfacial atomic controlling has to be considered explicitly. Further, combinations with magnetic quantum dos or clusters are also expected [90]. Junction with graphene is also anticipated [91].

(ii) Since the Heusler alloys are basically formed as body- or face-centered cubic structures, a crystalline symmetry is relatively high in the bulk form. Not only ordering controlling but also active controlling of strain and designing the quantized states pave a way for creation of novel concepts. In fact, the quantized states in hetero-structures are observed in resonant TMR bias-dependent measurements [92].

(iii) Novel physics can be developed using Heusler alloys. Due to the flexible tuning of band structures, semi-metallic and Weyl-type band crossings are anticipated. These are discussed by Berry curvature [93], which affects the anomalous Hall effects.

(iv) As for the material design, the machine learning procedures for alloy compounds are also helpful techniques. With accelerating the designing of

band structures, quantum materials exhibiting topological phenomena and spin-thermal conversion effects are modified.

For probing the electronic structures, spin states, and orbital states, not only XMCD but also other techniques are also developed. The element-specific characterization is a powerful technique. X-ray magnetic linear dichroism with an element-specific characterization is also a powerful technique for the estimation of magnetic anisotropy and quadrupole moments using magneto-optical sum rules in the same manner as those in XMCD. The x-ray magnetic spectroscopy and microscopy during the bias applying are also strongly demanded. Further, to detect the spin-resolved band structures directly, high-resolution spin- and orbital-resolved photoemission spectroscopy has to be also developed with high efficiency.

Acknowledgements The authors acknowledge to the collaboration with Dr. Tomoki Tsuchiya, Dr. Lakhan Bainsla in Tohoku University for the part of Sect. 10.3.1 and 10.3.2 and with Dr. Yoshio Miura in National Institute for Materials Science (NIMS) for Sect. 10.3.3. The authors acknowledge the fruitful discussion with Dr. Seiji Mitani in NIMS. These works are partly supported by KAKENHI (16H06332) and CREST (JPMJCR17J5). Synchrotron radiation experiments were performed under the approval of the Photon Factory Program Advisory Committee, KEK (Nos. 2017G060 and 2019G028).

References

1. H.S. Bennett, E.A. Stern, Phys. Rev. **137**, 448 (1965)
2. J.L. Erskine, E.A. Stern, Phys. Rev. B **12**, 5016 (1975)
3. G. Schütz, W. Wagner, W. Wilhelm, P. Kienle, R. Zeller, R. Frahm, G. Materlik, Phys. Rev. Lett. **58**, 737 (1987)
4. C.T. Chen, F. Sette, Y. Ma, S. Modesti, Phys. Rev. B **42**, 7262 (1990)
5. B.T. Thole, P. Carra, F. Sette, G. van der Laan, Phys. Rev. Lett. **68**, 1943 (1992)
6. P. Carra, B.T. Thole, M. Altarelli, X. Wang, Phys. Rev. Lett. **70**, 694 (1993)
7. C.T. Chen, Y.U. Idzerda, H.-J. Lin, N.V. Smith, G. Meigs, E. Chaban, G.H. Ho, E. Pellegrin, F. Sette, Phys. Rev. Lett. **75**, 152 (1995)
8. T. Kinoshita, K. Arai, K. Fukumoto, T. Ohkochi, M. Kotsugi, F. Guo, T. Muro, T. Nakamura, H. Osawa, T. Matsushita, T. Okuda, J. Phys. Soc. Jpn. **82**, 021005 (2013)
9. A. Kirilyuk, A.V. Kimel, T. Rasing, Rev. Mod. Phys. **82**, 2731 (2010)
10. J. Okabayashi, Y. Miura, T. Taniyama, npj Quantum Mater. **4**, 21 (2019)
11. H.A. Bethe, E.E. Salpeter, *Quantum Mechanics of One-and Two-Electron Atoms.* (Springer, Berlin, 1957)
12. M. Weissbluth, *Atoms and Molecules* (Academic Press, New York, 1978).
13. J. Stöhr, H.C. Siegmann, Magetism (Springer, Berlin, 2006)
14. F. Heusler, Verh. Dtsch. Phys. Ges. **5**, 219 (1903)
15. A. Hirohata, H. Sukegawa, H. Yanagihara, I. Žutic, T. Seki, S. Mizukami, R. Swaminathan, IEEE Trans. Mag. **51** 0800511 (2015)
16. T. Graf, C. Felser, S.S.P. Parkin, Progress in Solid State Chem. **39**, 1 (2011)
17. Y. Sakuraba, M. Hattori, M. Oogane, Y. Ando, H. Kato, A. Sakuma, T. Miya-zaki, H. Kubota, Appl. Phys. Lett. **88**, 192508 (2006)
18. S. Tsunegi, Y. Sakuraba, M. Oogane, K. Takanashi, Y. Ando, Appl. Phys. Lett. **93**, 112506 (2008)

19. N. Tezuka, N. Ikeda, F. Mitsuhashi, S. Sugimoto, Appl. Phys. Lett. **94**, 1 (2009)
20. W. Wang, H. Sukegawa, R. Shan, S. Mitani, K. Inomata, Appl. Phys. Lett. **95**, 182502 (2009)
21. A. Rajanikanth, Y.K. Takahashi, K. Hono, J. Appl. Phys. **105**, 063916 (2009)
22. L. Bainsla, A.I. Mallick, M.M. Raja, A.K. Nigam, B.S.DCh.S. Varaprasad, Y.K. Takahashi, A. Alam, K.G. Suresh, K. Hono, Phys. Rev. B **91**, 104408 (2015)
23. B. Hu, K. Moges, Y. Honda, H.X. Liu, T. Uemura, M. Yamamoto, J.I. Inoue, M. Shirai, Phys. Rev. B **94**, 094428 (2016)
24. Y. Miura, K. Abe, M. Shirai, Phys. Rev. B **83**, 214411 (2011)
25. M. Lezaic, P. Mavropoulos, J. Enkovaara, G. Bihlmayer, S. Bl¨ugel, Phys. Rev. Lett. **97**, 026404 (2006)
26. K. Nawa, Y. Miura, RSC Adv. **9**, 30462 (2019)
27. I. Galanakis, P.H. Dederichs, and N. Papanikolaou Phys. Rev. B **66**, 174429 (2002)
28. R.A. de Groot, F.M. Mueller, P.G. van Engen, K.H.J. Buschow, Phys. Rev. Lett. **50**, 2024 (1983)
29. J. Okabayashi, A. Kimura, O. Rader, T. Mizokawa, A. Fujimori, T. Hayashi, M. Tanaka, Phys. Rev. B **64**, 125304 (2001)
30. J. Okabayashi, T. Mizokawa, D.D. Sarma, A. Fujimori, T. Slupinski, A. Oiwa, H. Munekata, Phys. Rev. B **65**, 161203(R) (2002)
31. S. Mizukami, A. Sakuma, A. Sugihara, K.Z. Suzuki, R. Ranjbar, Scripta Mater. **118**, 70 (2016)
32. J. Kübler, C. Felser, Eur. Phys. Lett. **114**, 47005 (2016)
33. K. Manna, Y. Sun, L. Muechler, J. Kübler, C. Felser, Nat. Rev. Mater. **3**, 244 (2018)
34. M. Hirschberger, S. Kushwaha, Z. Wang, Q. Gibson, S. Liang, C.A. Belvin, B.A. Bernevig, R.J. Cava, N.P. Ong, Nature Materials **15**, 1161 (2016)
35. K. Amemiya, H. Kondoh, T. Yokoyama, T. Ohta, J. Electron Spectrosc. Relat. Phenom. **124**, 151 (2002)
36. X. Dai, G. Liu, G.H. Fecher, C. Felser, Y. Li, H. Liu, J. Appl. Phys. **105**, 07E901 (2009)
37. L. Bainsla, A.I. Mallick, M. Manivel Raja, A.K. Nigam, B.S.D.C.S. Varaprasad, Y.K. Takahashi, A. Alam, K.G. Suresh, K. Hono, Phys. Rev. B **91**, 104408 (2015)
38. G.Z. Xu, E.K. Liu, Y. Du, G.J. Li, G.D. Liu, W.H. Wang, G.H. Wu, Europhys. Lett. **102**, 17007 (2013)
39. V. Alijani, S. Ouardi, G.H. Fecher, J. Winterlik, S.S. Naghavi, X. Kozina, G. Stryganyuk, C. Felser, Phy. Rev. B **84**, 224416 (2011)
40. K. Ozdogan, E. Sasioglu, I. Galanakis, J. Appl. Phys. **113**, 193903 (2013)
41. P. Klaer, B. Balke, V. Alijani, J. Winterlik, G.H. Fecher, C. Felser, H.J. Elmers, Phys. Rev. B **84**, 144413 (2011)
42. E. Goering, Philos. Mag. **85**, 2895 (2005)
43. A. Scherz, H.Wende, C. Sorg, K. Baberschke, J.Minr, D. Benea, H. Ebert, Phys. Scr., T **115**, 586 (2005)
44. Y. Feng, H. Chen, H. Yuan, Y. Zhou, X. Chen, J. Magn. Magn. Mater. **378**, 7 (2015)
45. L. Bainsla, R. Yilgin, J. Okabayashi, A. Ono, K.Z. Suzuki, S. Mizukami, Phys. Rev. B **96**, 094404 (2017)
46. L. Bainsla, A.I. Mallick, A.A. Coelho, A.K. Nigam, B.S.DCh.S. Varaprasad, Y.K. Takahashi, A. Alam, K.G. Suresh, K. Hono, J. Magn. Magn. Mater. **394**, 82 (2015)
47. Y. Jin, P. Kharel, S.R. Valloppilly, X.-Z. Li, D.R. Kim, G.J. Zhao, T.Y. Chen, R. Choudhary, A. Kashyap, R. Skomski, D.J. Sellmyer, Appl. Phys. Lett. **109**, 142410 (2016)
48. Y. Jin, R. Skomski, P. Kharel, S.R. Valloppilly, D.J. Sellmyer, AIP Adv. **7**, 055834 (2017)
49. R. Choudhary, P. Kharel, S.R. Valloppilly, Y. Jin, A. O'Connell, Y. Huh, S. Gilbert, A. Kashyap, D.J. Sellmyer, R. Skomski, AIP Adv. **6**, 056304 (2016)
50. Y. Sakuraba, J. Nakata, M. Oogane, H. Kubota, Y. Ando, A. Sakuma, T. Miyazaki, Jpn. J. Appl. Phys. **44**, 6535 (2005)
51. K. Kobayashi, R. Kainuma, K. Ishida, Mater. Trans. **47**, 20 (2006)
52. T. Tsuchiya, T. Roy, K. Elphick, J. Okabayashi, L. Bainsla, T. Ichinose, K.Z. Suzuki, M. Tsujikawa, M. Shirai, A. Hirohata, S. Mizukami, Phys. Rev. Mater. **3**, 084403 (2019)
53. B. Dieny, M. Chshiev, Rev. Mod. Phys. **89**, 025008 (2017)
54. S. Fukami, C. Zhang, S. DuttaGupta, A. Kurenkov, H. Ohno, Nat. Mater. **15**, 535 (2016)

55. X. Marti, I. Fina, C. Frontera, Jian Liu, P. Wadley, Q. He, R. J. Paull, J. D. Clarkson, J. Kudrnovsky, I. Turek, J. Kune?, D. Yi, J-H. Chu, C. T. Nelson, L. You, E. Arenholz, S. Salahuddin, J. Fontcuberta, T. Jungwirth, R. Ramesh, Nat. Mater. **13**, 367 (2014).
56. J. Okabayashi, Y. Miura, H. Munekata, Sci. Rep. **8**, 8303 (2018)
57. J.W. Koo, S. Mitani, T.T. Sasaki, H. Sukegawa, Z.C. Wen, T. Ohkubo, T. Niizeki, K. Inomata, K. Hono, Appl. Phys. Lett. **103**, 192401 (2013)
58. J. Okabayashi, J.W. Koo, H. Sukegawa, S. Mitani, Y. Takagi, T. Yokoyama, Appl. Phys. Lett. **105**, 122408 (2014)
59. J. Okabayashi, Y. Iida, Q. Xiang, H. Sukegawa, S. Mitani, Appl. Phys. Lett. **115**, 252402 (2019)
60. S. Mizukami, F. Wu, A. Sakuma, J. Walowski, D. Watanabe, T. Kubota, X. Zhang, H. Naganuma, M. Oogane, Y. Ando, T. Miyazaki, Phys. Rev. Lett. **106**, 117201 (2011)
61. S. Mizukami, T. Kubota, F. Wu, X. Zhang, T. Miyazaki, H. Naganuma, M. Oogane, A. Sakuma, Y. Ando, Phys. Rev. B **85**, 014416 (2012)
62. D. Kim, J. Hong, L. Vitos, Phys. Rev. B **90**, 144413 (2014)
63. K. Rode, N. Baadji, D. Betto, Y.-C. Lau, H. Kurt, M. Venkatesan, P. Stamenov, S. Sanvito, J.M.D. Coey, Phys. Rev. B **87**, 184429 (2013)
64. M. Glas, C. Sterwerf, J.M. Schmalhorst, D. Ebke, C. Jenkins, E. Arenholz, G. Reiss, J. Appl. Phys. **114**, 183910 (2013)
65. D. Oshima, M. Tanimoto, T. Kato, Y. Fujiwara, T. Nakamura, Y. Kotani, S. Tsunashima, S. Iwata, IEEE Trans. Magn. **52**, 1 (2016)
66. J. Okabayashi, in *Progress in Photon Science II*, ed. by K. Yamanouchi, S. Tunik, V. Makarov (Springer Nature Switzerland AG, 2019), p. 471.
67. J.A. Moyer, C.A.F. Vaz, D.A. Arena, D. Kumah, E. Negusse, V.E. Henrich, Phys. Rev. B **84**, 054447 (2011)
68. K.Z. Suzuki, R. Ranjbar, J. Okabayashi, Y. Miura, A. Sugihara, H. Tsuchiura, S. Mizukami, Sci. Rep. **6**, 30249 (2016)
69. P. Bruno, Phys. Rev. B **39**, 865(R) (1989)
70. G. van der Laan, J. Phys.: Condens. Matter **10**, 3239 (1998)
71. D. Wang, R. Wu, A.J. Freeman, Phys. Rev. B **47**, 14932 (1993)
72. J. Stöhr, H. Konig, Phys. Rev. Lett. **75**, 3748 (1995)
73. Y. Kota, A. Sakuma, J. Phys. Soc. Jpn. **83**, 034715 (2014)
74. J. Okabayashi, Y. Miura, Y. Kota, K. Z. Suzuki, A. Sakuma, S. Mizukami, Sci. Rep. **10**, 9744 (2020)
75. V. Alijani, J. Winterlik, G.H. Fecher, C. Felser, Appl. Phys. Lett. **99**, 222510 (2011)
76. S. Chadov, J. Kiss, C. Felser, Adv. Funct. Mater. **23**, 832 (2013)
77. T. Kubota, Y. Miura, D. Watanabe, S. Mizukami, F. Wu, H. Naganuma, X. Zhang, M. Oogane, M. Shirai, Y. Ando, Appl. Phys. Express **4**, 043002 (2011)
78. Q.L. Ma, T. Kubota, S. Mizukami, X.M. Zhang, H. Naganuma, M. Oogane, Y. Ando, T. Miyazaki, Phys. Rev. B **87**, 184426 (2013)
79. R. Ranjbar, K. Suzuki, A. Sugihara, Q.L. Ma, X.M. Zhang, Y. Ando, T. Miyazaki, S. Mizukami, Mater. Des. **96**, 490 (2016)
80. S. Mao, J. Lu, X. Zhao, X. Wang, D. Wei, J. Liu, J. Xia, J. Zhao, Sci. Rep. **7**, 43064 (2017)
81. S. Mizukami, T. Kubota, S. Iihama, R. Ranjbar, Q. Ma, X. Zhang, Y. Ando, T. Miyazaki, J. Appl. Phys. **115**, 17C119 (2014)
82. Q.L. Ma, S. Mizukami, T. Kubota, X.M. Zhang, Y. Ando, T. Miyazaki, Phys. Rev. Lett. **112**, 157202 (2014)
83. Q.L. Ma, X.M. Zhang, T. Miyazaki, S. Mizukami, Sci. Rep. **5**, 7863 (2015)
84. K. Minakuchi, R.Y. Umetsu, K. Kobayashi, M. Nagasako, R. Kainuma, J. Alloys Compd. **645**, 577 (2015)
85. S. Banerjee, W.L. O'Brien, B.P. Tonner, J. Magn. Magn. Mater. **198–199**, 267 (1999)
86. S. Ener, J. Kroder, K.P. Skokov, O. Gutfleisch, J. Alloys Compd. **683**, 198 (2016)
87. J. Okabayashi, K.Z. Suzuki, S. Mizukami, J. Magn. Magn. Mater. **460**, 418 (2018)
88. J. Okabayashi, H. Sukegawa, Z. Wen, K. Inomata, S. Mitani, Appl. Phys. Lett. **103**, 102402 (2013)

89. Z. Wen, J.P. Hadorn, J. Okabayashi, H. Sukegawa, T. Ohkubo, K. Inomata, S. Mitani, K. Hono, Appl. Phys. Express **10**, 013003 (2016)
90. J. Okabayashi, M. Mizuguchi, K. Ono, M. Oshima, A. Fujimori, H. Kuramochi, H. Akinaga, Phys. Rev. B **70**, 233305 (2004)
91. S. Li, K.V. Larionov, Z.I. Popov, T. Watanabe, K. Amemiya, S. Entani, P.V. Avramov, Y. Sakuraba, H. Naramoto, P.B. Sorokin, S. Sakai, Adv. Mater. **32**, 1905734 (2020)
92. Q. Xiang, H. Sukegawa, M. Belmoubarik, M. Al-Mahdawi, T. Scheike, S. Kasai, Y. Miura, S. Mitani, Advanced Science. **6**, 1901438 (2019)
93. J. Kubler, C. Felser, Phys. Rev. B **85**, 012405 (2012)